GENERAL PURPOSE PHOTOCATALYTIC REACTOR MODEL

Carlos Macías Gállego

PROYMATICA 21 S.L. Astrónoma Cecilia Payne s/n, Ed. Aldebarán M9.1. Parque Científico-Tecnológico Rabanales 21. 14014 Córdoba

Alejandro Cifuentes López

Addlink Software Científico

Abstract. the present work proposes a general-purpose photocatalytic reactor designed and implemented in COMSOL MULTYPHYSICS and that this implementation can be proved to be a useful tool for modelling and design photoreactor devices for different applications and chemical processes, from photodegradation to photosynthesis of valuable compounds. To this aim, a model of a catalytic photoreactor has been built in COMSOL and its efficiency in phenol degradation is tested through simulation in different conditions of light emission power, catalyst content, inlet concentration and space velocity.

.

I. INTRODUCTION

Photooxidation processes (POP) have been subjected to intensive research since the last four decades and are currently used for water treatment. POPs can be performed in homogeneous phase, inducing the formation of active radical species by direct photolysis of dissolved peroxides, like H_2O_2 or in a heterogeneous phase, in which radicals are induced through a solid catalyst. Heterogeneous Photocatalytic oxidation (HPO) comprises a set of technologies in which a solid catalyst, usually a broad band-gap semi-conductor material like TiO_2, generates electron-hole pairs by photon excitation, being those holes used for direct oxidation or for the generation of radical species [1], which in turn are responsible of organic contaminants degradation [2].

HPO technology can be classified in two groups: slurry-type reactors and immobilized type reactors (fig.1). In the first, the photocatalyst is dispersed as micro or nanoparticles in the liquor to be treated, being separated in a downstream unit and recycled back into the process. In the second, the catalyst is supported in a solid which can adopt different shapes and is immobilized in the reactor. The first type has the advantage of a larger surface per unit volume exposure but the drawbacks of radial light intensity decay due to strong scattering/absorption and the need of a downstream process to recover the catalyst, usually expensive and difficult to manage [3]. The fixed bed reactor avoids this drawback, but at the cost of a significant smaller surface exposure and higher head-loss, which could be critical, especially in gas phase reactors. Since the emitted light is rapidly absorbed in the fixed bed due to the shape and distribution of the solid supports, only a small fraction of the active material is used in the process giving place to low degradation rate-to-catalyst ratios. To increase this efficiency index, an HPO reactor design is proposed in which the active material is cast onto the solid support in a thin layer of micron order thickness, which is exposed directly to a light source. This configuration allows for almost a 100% exposure of the active material and can be applied either in flat surface or annular-type reactors allowing for different support geometric designs to increase the exposed surface to volume ratio (fig. 1). This kind of thin film coated HPO devices has been tested in flat reactors irradiated with sunlight for water [4] or air [5] decontamination, in annular photoreactors with peripheral radiation source [6] but not in annular thin films with inner surface thin film-coated with concentric radiation source.

The full modeling of heterogeneous photocatalytic reactors requires to couple several physical phenomena to simulate processes occurring inside the reactor. Those are (a) radiation emission and incidence, (b) radiation absorption and scattering, (c) photoconversion kinetics, (d) heat transfer and (e) hydrodynamics and transport phenomena. These physics are strongly coupled (see fig. 9). For example, the chemical kinetics is a function of local radiation absorption, which is in turn a function of catalyst characteristics, reactor geometry and transport phenomena.

Several papers on simulation of POP and HPO devices have been published so far. Regarding the radiation part of the physics, Cabrera et al solved the radiation transfer equation (RTE) to compute the scattering and absorption coefficients of TiO_2 suspension from experimental measurements [7], Pareek et al [8] solved the RTE for several slurry type reactor configurations, Alvarado et al [9] solved the RTE with scattering and absorption in an annular slurry type batch photoreactor by discrete ordinate and Monte Carlo methods, and tested the impact of the radiant field on the reaction kinetics of the oxidation of benzyl alcohol to benzaldehyde using COMSOL and Elyasi et al described a general procedure for simulating radiant fields with measured boundary values [10]. From a fluid dynamics perspective, there are several works applying CFD techniques to solve the species concentration field coupled with flow field in continuous flow photoreactors of the slurry type [11] and fixed bed or monolith type [3, 6, 12-14]. From the chemical kinetics perspective, several models have been applied to photo reaction mechanisms, from light intensity dependent n-order [4, 9, 11] and Langmuir-Hinshelwood [12-14] kinetics, to more developed specific equations [3,15].

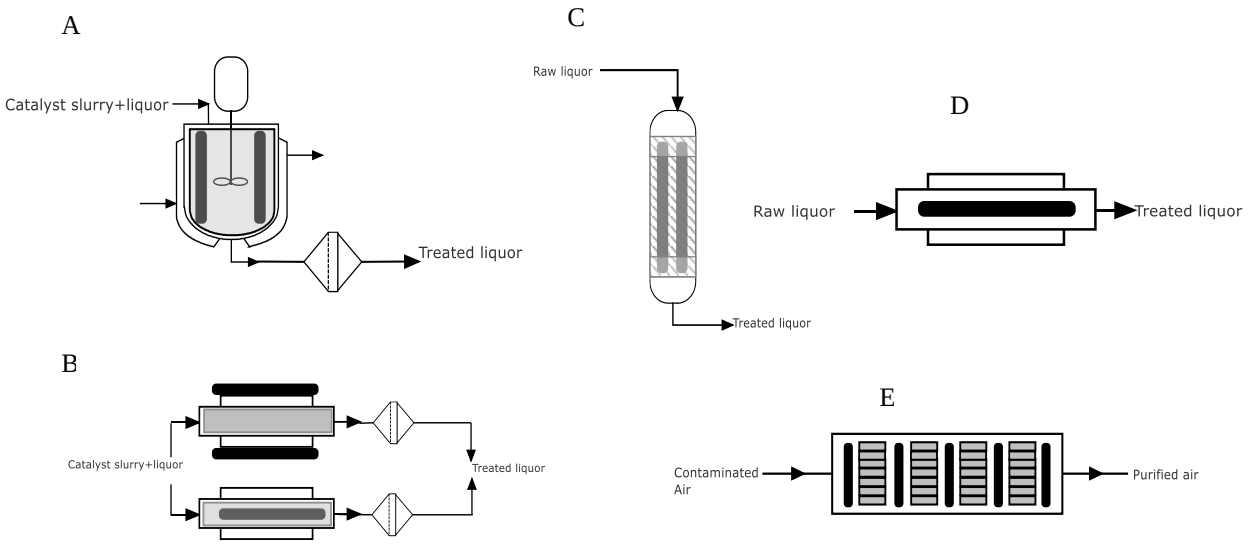

Figure 1.- HPO devices. Left: slurry type HPO; Slurry Batch or CSTR (A), Slurry Flow through (B). Right: immobilized type; packed column (C), annular thin-film (D) and honeycomb monolith (E).

In the present work, a multyphysics model of organic contaminants HPO on TiO_2, based on the Tourchi-Ollis reaction mechanism [2] with modified kinetics [15] is proposed, supplying a theoretical framework and an engineering tool based on multyphysics modelling and simulation, which can be useful in providing insights into interrelations of unit performance with geometry, operational parameters and catalyst material, and in design optimization of HPO units.

II. MATERIALS AND METHODS

Experimental setup

In the present work a fixed bed photocatalytic annular reactor (FBPAR) is simulated and the efficiency of the design is tested against phenol contaminated water. A description is shown in fig. 2. The FBPAR has a tubular geometry in which the inner surface consists of a monolithic catalyst support coated with a few microns thin film of TiO_2 nanoparticles which acts as photocatalyst and a source of (UV) light is located in the axial direction. The raw liquor passes through the reactor tube in a continuous flow. The specifications are shown in table AII2.

Several experimental conditions have been set to test the influence of different operational parameters on phenol degradation efficiency. The parameters tested are the lamp power, catalyst surface concentration, space velocity and phenol concentration. The different combinations are described in the results section.

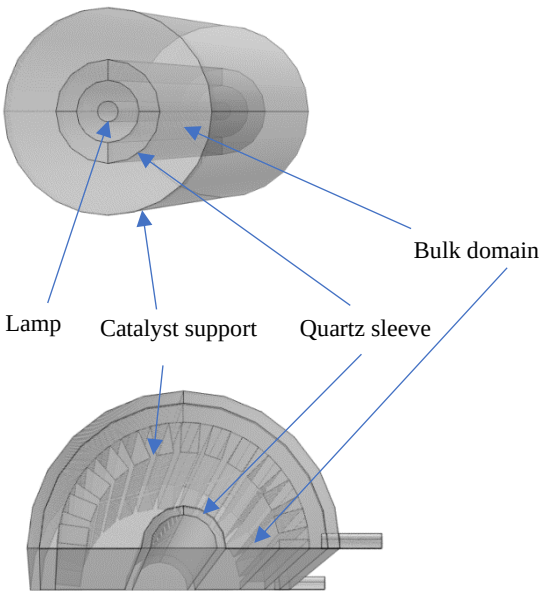

Figure 2.- Photochemical fixed bed annular reactor configuration. Simple axisymmetric plain geometry (left) and complex catalyst support geometry (right). Radiation source is in the center of the reactor.

The model is described first using a 0D component in which the chemical reaction mechanism (fig.1) is setup. Then, a 3D model generation node is added to this component and component 1 is generated with the described chemistry. All the computations are performed in this 3D component which is endowed with the geometry described in figure 1a, with different materials in the corresponding domains and with the different physics to account for the different variables of interest.

Global definitions

A first node of global definitions is setup in where all the global parameters of the model are defined. The parameters are classified in 4 groups: reactor parameters, reaction parameters, catalyst parameters, operation parameters and transport parameters. The values used for the simulations are specified in tables AII1 to AII5.

Geometry

The geometry in component 1 consists on 4concentric cylinders and is described in fig.3 with the different geometrical parts.

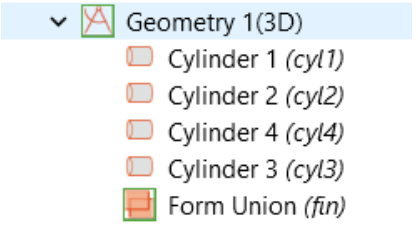

Figure 3.- Photoreactor 3D geometry

Materials

Four different materials have been assigned to the corresponding domains and boundaries:

- Perfect vacuum (sleeve and lamp interiors and reactor exterior
- Water (reaction chamber)
- Titanium dioxide nanoparticles (reactor inner boundary)
- Quartz (sleeve)

The material nodes hold all the parameter values needed for the laminar flow, heat transfer and geometrical optics modules. Fig. 4 shows the distribution of the different materials in the device.

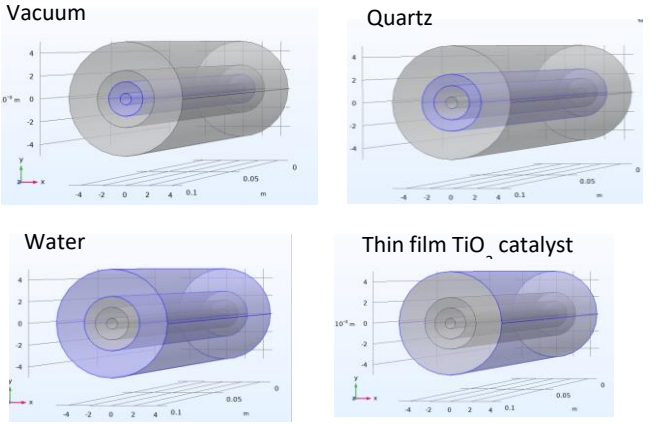

Figure 4.- Materials distribution

Physics modules

The reactor has been simulated with COMSOL in a model integrated by the following physics:

- Chemical reaction engineering, to specify the reaction mechanisms and kinetics of surface and bulk reactions
- Transport of diluted species, to specify the concentration distribution of species in space (and time).
- Laminar flow, to specify the convective transport term of species
- Ray optics/Geometrical optics, to specify the incident photon rate pattern which determines the catalyst surface activity.
- Heat transfer to specify heat dissipation and temperature effect on the chemical kinetics and temperature distribution in the reaction media.

The following features have been included in each module:

Chemical reaction engineering

A one irreversible reaction is included

$$TiO_2 + Ph \rightharpoonup TiO_2 + S \qquad (r13)$$

which represents a lumped mechanism of the reaction set in table 1 as described in section 2.1. In the chemical reaction feature, the kinetic equation 8 is introduced.

This module, incorporates a 3D model generation feature to translate the reactions set to the reactor geometry as explained below.

Laminar flow

The laminar flow module includes the default features plus inflow and outflow nodes.

Ray Optics

This module features fluence rate calculation and a release from boundary interfaces. The fluence rate calculation is needed to compute the volumetric rate of photon absorption by the catalyst and the release from boundary is needed to set up the ray emission pattern (fig. 4)

An upper limit of 10000 rays per release has been set as optimal to get a good accuracy and avoid ray-mesh interaction errors.

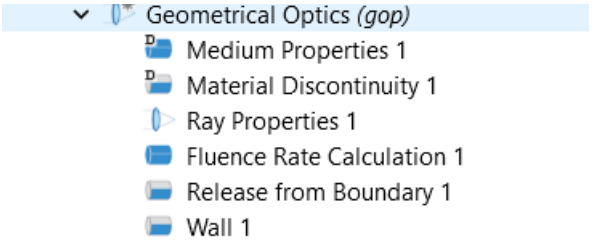

Figure 4.- Photochemical fixed bed annular reactor configuration. Simple axisymmetric plain geometry (left) and complex catalyst support geometry (right). Radiation source is in the center of the reactor.

Transport of diluted species

A transport of diluted species module has been included in the model to compute the species concentration in the reactor, taking inputs from the chemistry and laminar flow modules.

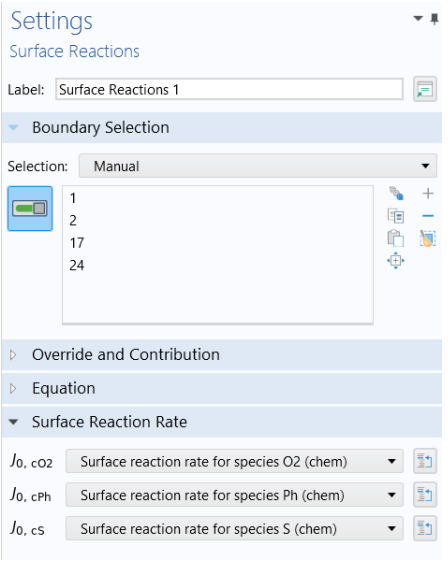

Figure 5.- Surface reactions node settings

The module includes the default features plus inflow and outflow nodes and special surface reactions node, which accounts for the reactions described in the chemist module and the boundaries where the reactions take place (inner reactor surface). Figure 5 shows the settings of the surface reactions feature in the transport of diluted species node.

Heat transfer

The heat transfer module, includes the default nodes plus inflow, outflow and a boundary heat source to account for the heat of reaction at the inner boundaries where the

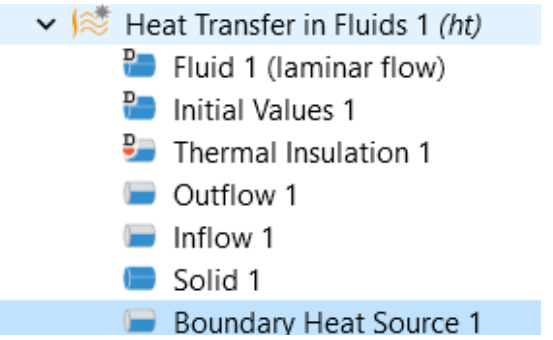

Figure 6.- Heat transfer module features

photocatalytic degradation takes place. Unfortunately, with this configuration it is not possible to account for the ray heating which should supply a positive heat source at the boundaries to compensate for the endothermic reactions. In this situation, the temperature plot on the reactor surface will show a T decrease along its length as photodegradation takes place and, as this decrease in T does not affect the reaction rates, since there is no physical connection in this model between T and reaction rate constants.

Meshing

The mesh should be enough fine to capture the finer geometric details while the density of rays should be in the order of the density of the finest mesh used in the model to prevent mesh elements with no ray contact yielding a null fluence rate at that point which is unphysical.

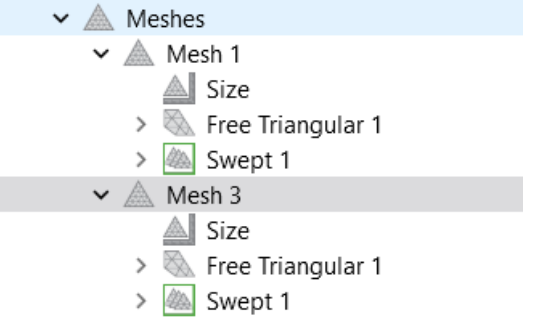

Figure 7.- Mesh node tree

Since the ray number per release is limited to 10000 in this model due to computational capacity, the mesh size is also conditioned to this number. For this reason, 2 meshes have been set for this model; one to solve the Geometrical optics and a finer mesh for the other physics (figs. 7 and 8).

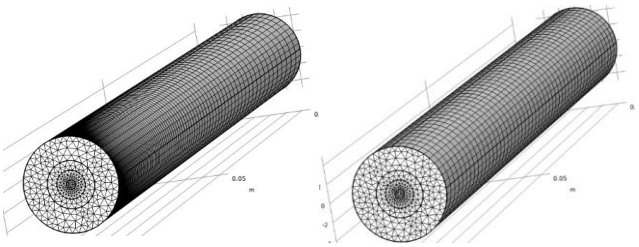

Figure 8.- Meshing details. Laminar flow, transport and heat transfer (left) and geometrical optics (right).

Studies

A time dependent study in the first place is set up to test the reaction engineering set. Once tested, the laminar flow and ray optics, have been tested in independent stationary studies to check their robustness. Another advantage is that the results of these 2 studies can be reused in the more coupled physics studies since their results are independent of the other physics results (fig.10). This saves a lot of time in the executions. Once tested, a parametric sweep for 10, 25, 50 and 100W lamp power for the ray optics study has been placed. The results of this study provide the information needed to study the power dependence of the phenol degradation and to perform the rest of the studies with a specific power selection if so wanted.

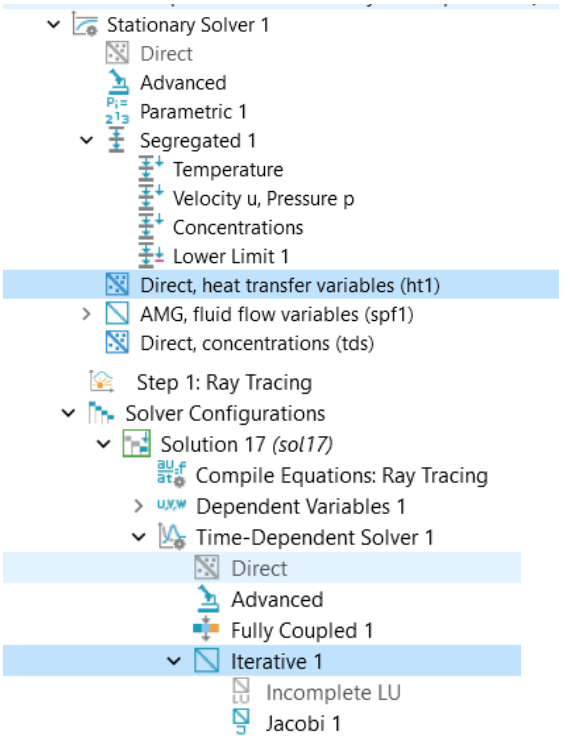

Figure 9.- Solver configuration for the Transport of diluted species parametric study and for the ray optics study.

To test the influence of catalyst, phenol concentrations and space velocity, the chemistry, transport, laminar flow and heat transfer models have been solved together in the same study, using the results of the Laminar flow and Geometrical optics as "variables not solved for" and needed for the solution of the transport of diluted species and chemist modules. This study is stationary, since this is a continuous device and the aim is to test the reactor efficiency in a steady regime. In this study, a parametric sweep node has been included to test the influence of the parameters mentioned above.

To test the influence of space velocity, a different study has been setup solving together the Laminar flow and transport of diluted species modules. The heat transfer module has been excluded since it adds a neglectable information at a high computational cost. Only in a couple of study 4 execution has been included to test the influence of power and space velocity as will be seen later.

Finally, a study with a power sweep has been set to test the influence of the power source on phenol degradation by obtaining the % degradation profiles along the reactor.

Unfortunately, the temperature dependence of the kinetics, could not be performed in this work due to the lack of information about the temperature dependence of individual kinetic constants in the reaction mechanism in table1 and in the simplified model.

For the ray optics and transport of diluted species parametric studies, the default solver configuration has been kept (fig.9).

Figure 10 shows the relationship between the different modules that integrate the model.

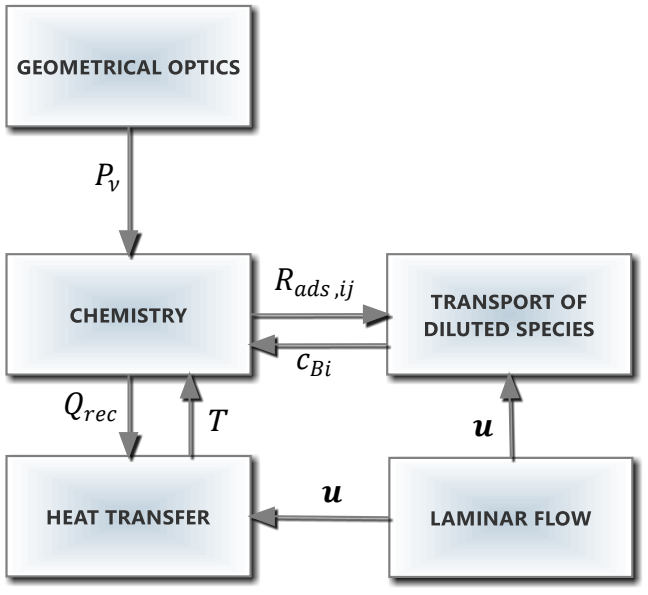

Figure 10.- Physics modules interrelationships and contributions scheme

Results configuration

In the results branch, the following plots and tables have been configured from the Datasets obtained by computing the studies explained in the former section:

- Fluence rate vs time
- Fluence rate vs power
- Ray trajectories
- Surface average fluence rates at different powers
- Fluence rate (surface plot)
- Phenol concentrations (surface plot)
- Phenol concentration (3D cut plane 2D plots)
- Reaction rates (surface plot)
- Phenol degradation (line plots)
- Reaction rates (line plot)

III. THEORY

1. General assumptions

In the model construction, the following assumptions have been made:

- The characteristic length, the catalyst layer thickness in this case, is at least 3 orders of magnitude larger than wavelength.
- Catalyst surface absorbs all the photons that reach the active surface.
- All photons absorbed contribute to the formation of an electron-hole pair.
- The surface of the catalyst is a porous media with a characteristic length, the particle diameter in this case, of the order of wavelength.
- Light scattering is negligible.
- Reactions by direct photolysis and direct oxidation are negligible [4], so surface reactions are the only ones considered in the model.
- The reactor operates in isothermal conditions.
- The photochemical process follows a Turchi-Ollis mechanism (R2-R12) [2, 15].
- All the adsorption sites are equal.

2. Model equations

Heterogeneous catalytic reactions and photoreactions and kinetic equations

For a heterogeneous catalytic reaction, the surface reaction rate R_s, can be expressed in general as [17]

$$R_{ads} = \frac{n_p}{c_{cat\_u} t} \qquad (1)$$

where n_p is the number of product moles, t is time and Cat_u is the measure unit of catalyst amount, which has following different unit bases:

- Active surface area of catalyst (m2)
- Unit mass of catalyst (kg)
- Unit volume of catalyst (m3)
- Active metal loading percentage

When photochemical processes are implied, the reaction mechanisms are more complex and need to take into account the photon absorption and the catalyst activation and deactivation processes. All these complex mechanisms implied, can be broken down into single reaction steps which are coupled in a reaction network. The mechanism which so far best describes photochemical processes in which a semiconductor-type catalyst like TiO_2 is implied is the one by Turchi and Ollis [2, 15] depicted in table 1

Activation	$\boldsymbol{TiO_2 \rightharpoonup TiO_2 + e^- + h^+}$	$(\boldsymbol{r1})$
Adsorption	$O_L^{2-} + Ti^{IV} + H_2O \leftrightharpoons O_LH^- + Ti^{IV} - OH^-$	$(r2a)$
	$Ti^{IV} + H_2O \leftrightharpoons Ti^{IV} - H_2O$	$(r2b)$
	$Ti^{IV} + Ph \leftrightharpoons Ti^{IV}\|Ph$	$(r3)$
	$HO^{\cdot} + Ti^{IV} \leftrightharpoons Ti^{IV}\|HO^{\cdot}$	$(r4)$
Recombination	$e^- + h^+ \rightharpoonup heat$	$(r5)$
Hole trapping	$Ti^{IV} - OH^- + h^+ \rightharpoonup Ti^{IV}\|HO^{\cdot}$	$(r6a)$
	$Ti^{IV} - H_2O + h^+ \rightharpoonup H^+ + Ti^{IV}\|HO^{\cdot}$	$(r6b)$
	$Ti^{IV}\|Ph + h^+ \leftrightharpoons Ti^{IV}\|Ph^+$	$(r7)$
Electron trapping	$e^- + Ti^{IV} \leftrightharpoons Ti^{III}$	$(r8a)$
	$O_2 + Ti^{III} \leftrightharpoons Ti^{IV} - O_2^-$	$(r8b)$
Hydroxyl attack	$Ti^{IV}\|HO^{\cdot} + Ti^{IV}\|Ph \rightharpoonup Ti^{IV} + Ti^{IV}\|S$	$(r9)$
	$HO^{\cdot} + Ti^{IV}\|Ph \rightharpoonup Ti^{IV}\|S$	$(r10)$
	$Ti^{IV}\|HO^{\cdot} + Ph \rightharpoonup Ti^{IV} + S$	$(r11)$
	$HO^{\cdot} + Ph \leftrightharpoons S$	$(r12)$

Table 1.- Photoreaction mechanism for phenol degradation

This mechanism has been applied successfully to the degradation of phenol [15], but it is a very general mechanism which can be applied to the degradation of different organic compounds. S is a degradation product specie.

As table 1 shows, the different reactions comprising the mechanism are classified into 6 different groups attending the kind of process, which determine the kinetics as explained in the following subsections.

Activation reactions

This group describes the formation of electron-hole pairs, comprises reaction R1 and it is the only one in which light is implied. Its rate is modelled by the following equation [15]

$$r_g = \frac{\bar{\phi} P_v}{S_{BET} c_{cat} \beta} \qquad (2)$$

Adsorption reactions

This group describes the reversible adsorption of species from the bulk, comprises reactions r2 to r4. Its rate takes into account the adsorption isotherm which describes the equilibrium of adsorption and the mass transfer coefficient between the solid and the bulk and it is modelled by the following equations

$$R_{ads,i} = h_{ads,i}(c_{v,i} - c_{eq,i}) \qquad (3a)$$

where

$$c_{v,i} = S_A c_{ads,i} \qquad (3b)$$

$$c_{eq,i} = \rho_B c_{p,i} \qquad (3c)$$

and

$$c_{P,i} = f_{iso}(c_i) \qquad (3d)$$

being $f_{iso}(c_i)$ the adsorption isotherm for the specie i relating the equilibrium of specie i adsorbed with equilibrium concentration in the bulk.

Recombination

This group describes the recombination of electron-hole pairs, comprises reaction R5 and its product is heat due to vibrational electron relaxation. Its rate is modelled by the following simple first order process

$$R_r = k_{rec}[e^-][h^+] \qquad (4)$$

Holes trapping

This group describes the trapping of holes by adsorbed or surface species and its general expression is given by

$$R_{h,i} = k^f_{h,i} c_{ads,i}[h^+] - k^r_{h,i} c_{ads,i}[h^+] \quad (5)$$

Electron trapping

This group describes the trapping of electrons by adsorbed or surface species and its general expression is given by

$$R_{e,i} = k^f_{e,i} c_{ads,i}[e^-] - k^r_{e,i} c_{ads,i}[e^-] \quad (6)$$

Hydroxyl attack

This group describes the reaction between hydroxyl radicals and organic reactant and intermediates and comprise both adsorbed and bulk species. They are irreversible and their rate is modelled by the following simple first order process

$$R_{ads,ij} = k_{ads,ij} c_{ads,i} c_{ads,j} \qquad (7a)$$

$$R_{ads,B,ij} = k_{ads,B,ij} c_{ads,i} c_{B,j} \qquad (7b)$$

$$R_{B,ij} = k_{B,ij} c_{B,i} c_{B,j} \qquad (7c)$$

All rate constants in equations 4-7 are supposed to follow an Arrhenius temperature dependence.

All the equations above, except 7c, are applied only in the inner surface of the reactor, onto the catalytic layer.

The former reaction mechanism has a main drawback; it needs 22 rate constants to be specified for the mass action law to be applied in the reaction rate computations and many of them are not available or measured yet. Nevertheless, considering that the organic compound degradation rate is the variable of interest, the system of kinetic equations 3-7 can be simplified in only 1 equation with only 3 kinetic constants, under an [$^{\cdot}$OH] and [h^+] steady state assumption, and also assuming that the concentration of intrinsic charge carriers is equal, i.e [h^+] = [e^-] at any instant, leading to the following rate equation for the organic compound degradation [15]

$$r_{ph} = -S_{BET} c_{cat} \alpha_1 \frac{\alpha_{3,ph}[ph]}{(\alpha_{3,ph}[ph] + 1)} \left\{ \sqrt{1 + \frac{\alpha_2 F_{v,a}}{S_{BET} c_{cat}}} - 1 \right\} \qquad (8)$$

where α_1, α_2, and $\alpha_{3,ph}$ are rate constant derived under the above assumptions, which depend on the individual kinetic constants of the raw model and which can be experimentally adjusted.

Mass transport equations and laminar flow

The general governing equation of this model is the mass transport process of bulk species in free 3D isotropic medium is given by

$$\frac{\partial c_{Bi}}{\partial t} = -\boldsymbol{u}\nabla c_{Bi} - \nabla(D_i \nabla c_{Bi}) + R_j \qquad (9)$$

where R_j comprises all the source terms (kinetic rates) given in the previous section.

For a steady state case, eq. 9 becomes

$$-\boldsymbol{u}\nabla c_{Bi} - \nabla(D_{Bi} \nabla c_{Bi}) + R_j = 0 \qquad (10)$$

The flow speed $\boldsymbol{u}$ is defined by the Navier – Stokes equations in laminar flow (time dependent and stationary)

$$\frac{\partial \rho_B \boldsymbol{u}}{\partial t} + \boldsymbol{u}\nabla\rho\boldsymbol{u} = -\nabla p - \nabla \cdot \boldsymbol{\tau} + \rho_B \boldsymbol{F} \qquad (11a)$$

$$\boldsymbol{u}\nabla\rho\boldsymbol{u} = -\nabla p - \nabla \cdot \boldsymbol{\tau} + \rho_B \boldsymbol{F} \qquad (11b)$$

$$\nabla\rho\boldsymbol{u} = 0 \qquad (11c)$$

With the boundary conditions

$$\boldsymbol{u}|_{z=0} = u_{z\,inlet} \qquad (12a)$$

$$c_{Bi}|_{z=0} = c_{Bi0} \qquad (12c)$$

$$\nabla c_{Bi}|_{z=L} = 0 \qquad (12d)$$

Radiative transfer equations

The radiative energy of an electromagnetic beam through space and time for a particular frequency ν can be expressed as

$$dE = I_\nu dv cos\theta dA d\Omega dt \qquad (13)$$

The intensity of the beam is constant with distance unlike the flux which decreases with distance due to ray separation.

The light beam intensity can be defined as the volumetric energy density per solid angle times the speed of light c.

The Intensity, as is constant through distance, is considered the fundamental unit to define the radiation field. From intensity field, the energy flux can be computed.

The equation of radiative transfer says that as a beam of radiation travels, it loses energy to absorption, gains energy by emission processes, and redistributes energy by scattering. The differential form of the equation for radiative transfer is:

$$\frac{1}{c}\frac{\partial I_\nu}{\partial t} + \hat{\Omega}\nabla I_\nu + \left(k_{\nu,s} + k_{\nu,a}\right)\rho I_\nu = j_\nu \rho + \frac{1}{4\pi} k_{\nu,s}\rho \int_\Omega p(\Omega,\Omega') I_\nu d\Omega \qquad (14)$$

where c is the speed of light, j_ν is the emission coefficient, $k_{\nu,s}$ is the scattering opacity, $k_{\nu,a}$ is the absorption opacity, ρ is the mass density of the scatterer-absorber and the integral term represents radiation scattered from other directions, characterized by the solid angle Ω, onto a surface, being $p(\Omega,\Omega')$ the phase function describing the probability density of scattering between all possible pairs of solid angles.

Considering that the source of emission is constant, monochromatic and unique, and that the medium is homogeneous with isotropic scattering [16], equation 1 can be reduced to

$$\hat{\Omega}\nabla I_\nu + \left(k_{\nu,s} + k_{\nu,a}\right)\rho I_\nu = \frac{1}{4\pi} k_{\nu,s}\rho \int_\Omega I_\nu d\Omega \qquad (15)$$

The sum of the scattering opacity and the absorption opacity is the extinction coefficient and the ratio of the scattering opacity to the extinction coefficient is the scattering albedo coefficient which is inherent to each photocatalyst since it represents its photon absorption capacity.

In a medium without scattering like a clear liquid without particles, scattering can be neglected and all scattering terms disappear reducing 15 to

$$\hat{\Omega}\nabla I_\nu = -k_{\nu,a}\rho I_\nu \qquad (16)$$

which is the Lambert – Beer law of absorption.

The boundary condition of 15 is

$$I_\nu|_{r=0} = I_{\nu 0} \qquad (17)$$

with $I_{\nu 0}$ being the light intensity at the emission surface.

The fluence rate is defined at any point in a domain as the total incident power that would hit a small spherical target at that location, from all directions, divided by the cross-sectional area of the sphere [5]. So, once the radiation field is computed, the fluence rate can be computed as

$$F_\nu = 2\pi \int_{\mu=-1}^{\mu=1} I_\nu(x,\mu) d\mu \qquad (18)$$

With $\mu = cos\theta$ [4].

The volumetric rate of photons absorption (VRPA) is a variable of interest since it is directly related to the kinetics modulation. In the cases for which eq. 15 holds, VRPA is defined as

$$F_{\nu,a} = k_{\nu,a} 2\pi \int_{\mu=-1}^{\mu=1} I_\nu d\mu \qquad (19)$$

In the COMSOL model, this variable is identified with the fluence rate, which is computed by a special feature in the geometrical optics module. In the model, it is assumed that absorption coefficient $k_{\nu,a}$ is equal to 1 so $F_{\nu,a} \equiv F_\nu$.

By means of the ray optics module COMSOL computes the radiation intensity at each point in a different way than solving equation 15 with b.c. 17. Instead, COMSOL computes, with the Ray tracing study, the position and direction of a set of rays, starting from an initial ray release condition, explained in the former section. The position and direction and direction are denoted by the position vector **r** and the wave vector **k** and are given by

$$\frac{\partial \boldsymbol{r}}{\partial t} = \frac{\partial \omega}{\partial \boldsymbol{k}} \qquad (20a)$$

$$\frac{\partial \boldsymbol{k}}{\partial t} = -\frac{\partial \omega}{\partial \boldsymbol{r}} \qquad (20b)$$

Equations 20 give a good approximation to the RTE 15 solution when the wavelength of the rays are much smaller than the smallest geometrical detail in the model and are derived from the electromagnetic plane wave equation and considering the mathematical analogy with the relationship between the Lagrangian and Hamiltonian of a solid particle [17].

The ray tracing algorithm takes into account the interaction of rays with matter by means of the materials parameters and geometry meshing, to compute the changes in direction by material properties like refraction, reflection, absorption or scattering. In our model, only refraction in the 3 different domains and absorption at the inner boundaries are considered.

Considering the relationship between ω and $\boldsymbol{k}$ and in media where the refraction index is constant like in our model, we have $\frac{\partial \omega}{\partial \boldsymbol{r}} = 0$ and 20 are converted to

$$\frac{\partial \boldsymbol{r}}{\partial t} = \frac{c\boldsymbol{k}}{n|\boldsymbol{k}|} \qquad (21a)$$

$$\frac{\partial \boldsymbol{k}}{\partial t} = 0 \qquad (21b)$$

Now, the relative refraction index must be specified for each medium. In refractive index, a real component, defining the ratio between speed of light in vacuum and in the medium, and an imaginary part describing the electromagnetic loss, are defined. There is no interaction of light with materials except for the TiO_2 catalyst at the boundary, where all the hitting rays are absorbed and all the media here defined can be considered as isotropic so all the relative refractive indices are real scalars.

To solve eqs. 20, initial position and wavevector must be specified. The initial position can be defined in terms of the mesh, of a fixed grid or of the total number of rays released and the density distribution in the emitting boundary. The initial wave vectors can be defined by sampling from different ray distributions in each emission point. In this model, a total rays release of 10000 rays with a uniform density for the initial position and a Lambertian distribution for the initial wavevectors have been chosen (see materials and methods section).

Ray distribution reaches a steady state in some picoseconds and so happens with the fluence rate which depends on ray distribution. Fluence rate is based in the ray distribution, averaged over the mesh volume and is computed by

$$\frac{\partial F_v}{\partial t} = \frac{1}{V_m}\sum_i P_{vi} c_i \qquad (22)$$

where, P_{vi} and c_i are the ray power and the speed of light of ray i and V_m is the mesh volume. The mesh volume averaging is done to compensate for the tendency of larger domain element to intersect a greater number of rays [17].

Heat transfer equation

The incident light on the reactor walls produces some heating due to photon adsorption by electrons and electron-hole recombination by vibrational relaxation. The heat produced due to this process is a source term in the heat equation and is transferred to the moving fluid by conduction and convection. All these processes are coupled in the following equations

$$\rho_B C_p \frac{\partial T}{\partial t} + \rho_B C_p \boldsymbol{u}\nabla T + \nabla \cdot \boldsymbol{q} = Q_{rec} + Q_{rad} \qquad (23a)$$

$$\rho_B C_p \boldsymbol{u}\nabla T + \nabla \cdot \boldsymbol{q} = Q_{rec} + Q_{rad} \qquad (23b)$$

$$\boldsymbol{q} = -\kappa \nabla T \qquad (24)$$

$$Q_{rec} = R_r H_r \qquad (25)$$

Being Q_{rec} the heat flux by electron-hole pair recombination in reaction 4 and H_r the specific heat of the organic compound degradation reaction and Q_{rad} the heat released due to electron-hole recombination through vibrational relaxation process.

The boundary conditions are

$$T|_{z=0} = T_{in} \qquad (26)$$

Figure 2 shows the coupling between the different physics integrating the model.

VI. RESULTS AND DISCUSSION

The fluence rate is a measure of the amount of radiative energy reaching the catalyst surface per unit time. As stated in the assumptions in section 1, this is also the amount of energy absorbed by the catalyst, corresponding to the factor $P_{v,a}$ in equation 8. In Figure 11 is shown a plot of the fluence rate time dependence computed by the ray optics study. It can be seen that at 0.1 ns the fluence rate becomes steady, so fluence rate at this point in time will be taken as a reference value for all subsequent analysis

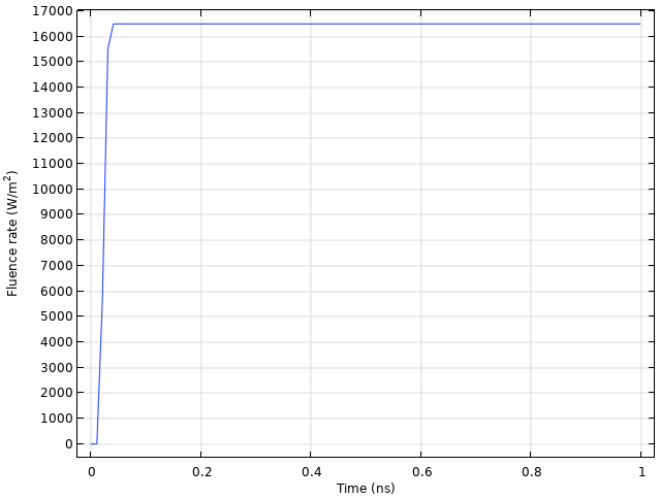

Figure 11.- Time dependence of the fluence rate with a 50W power lamp

P (W)	fluence rate·10^{-3} (W/m^2)
10	3.3623
25	8.4058
50	16.812
100	33.623

Table 2.- Fluence rate power dependence

In table 2 are shown the surface average fluence rate dependence on the lamp power and in figure 12 is shown the fluence rate distribution on the catalytic surface with a 25W lamp. It can be seen how the surface average fluence rate increases as power lamp increases with a completely linear dependence as expected.

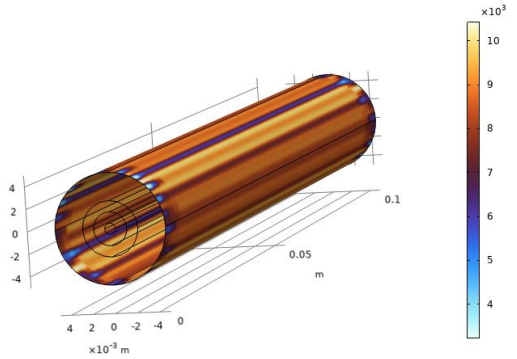

Figure 12.- Fluence rate surface distribution with a 25W power lamp

In the surface distribution, some inhomogeneity can be observed for all the lamp power tested, which is probably caused by the uneven computed ray distribution at that the surface distance.

Figure 14 shows the surface distribution of phenol concentration along the reactor and figure 15 shows the power dependence of phenol degradation %. In general, effects on the bulk solution are small in all cases but appreciable. This is due to the fact that the photocatalytic degradation is restricted to the inner reactor surface, meaning a low reaction area to bulk volume ratio, and the formation of a depleted diffusional layer that controls the whole process speed as can be seen in figure 13, where the diffusion layer tends to disappear when inlet flow is increased.

However, it can be seen how surface phenol is completely degraded in the first 30% of the reactor length with a 50W lamp, being this 100% degradation length not reached for 25 and 10W lamps. In those cases, maximum degradation reaches over 90% for the 25W lamp and over 80% for the 10W at 50% and 90% of reactor length respectively. Phenol degradation shows an appreciable sensitivity to the power lamp as can be concluded from the separation pattern of both the bulk and the surface concentration profiles.

Figure 16 shows the inlet concentration dependence of phenol degradation % for a 50W lamp power, 1300 kg/m^3 catalyst concentration and 1 min^{-1} space velocity. As in the previous case, the bulk concentration shows a smaller impact than the surface concentration which almost reach a 100% degradation of surface phenol. Phenol degradation shows a low sensibility to inlet concentration, since in bulk concentration all the profiles appear very close to each other while inlet concentration varies 15-fold. The same is observed

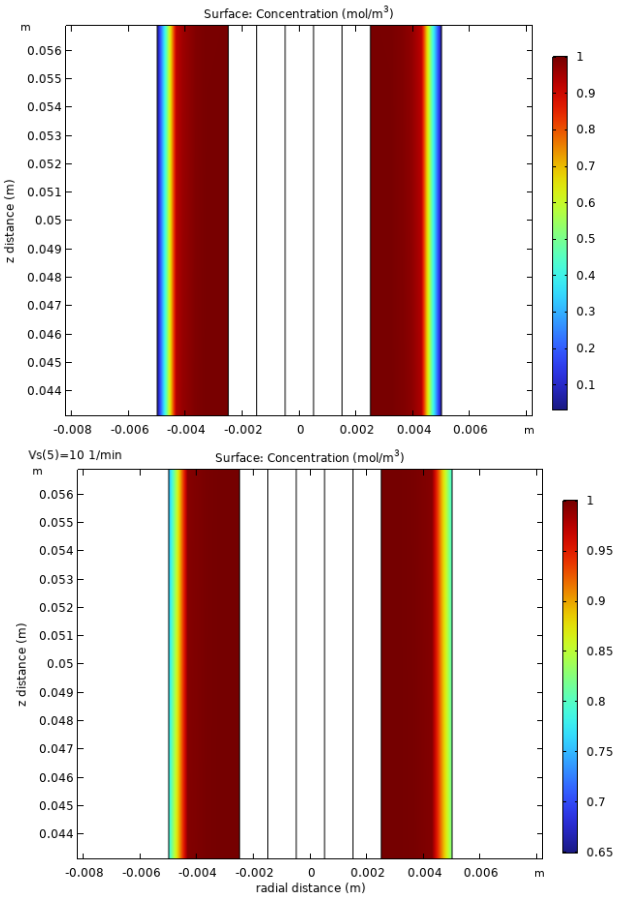

Figure 13.- Distribution of phenol concentration with a 50W power lamp with the diffusion layer (blue area) along reactor for a space pace velocity of 1 min^{-1} (up) and 10 min^{-1} (bottom)

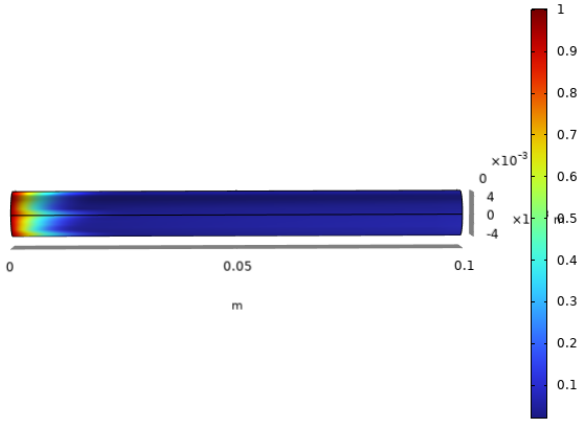

Figure 14.- Phenol surface distribution concentration. Conditions: inflow phenol concentration 1mmol/L; catalyst surface concentration 1300 kg/m^3; lamp power 50W, space velocity 1 min^{-1}

in the surface degradation rate except for the first 20% of reactor length where curves appear more separated.

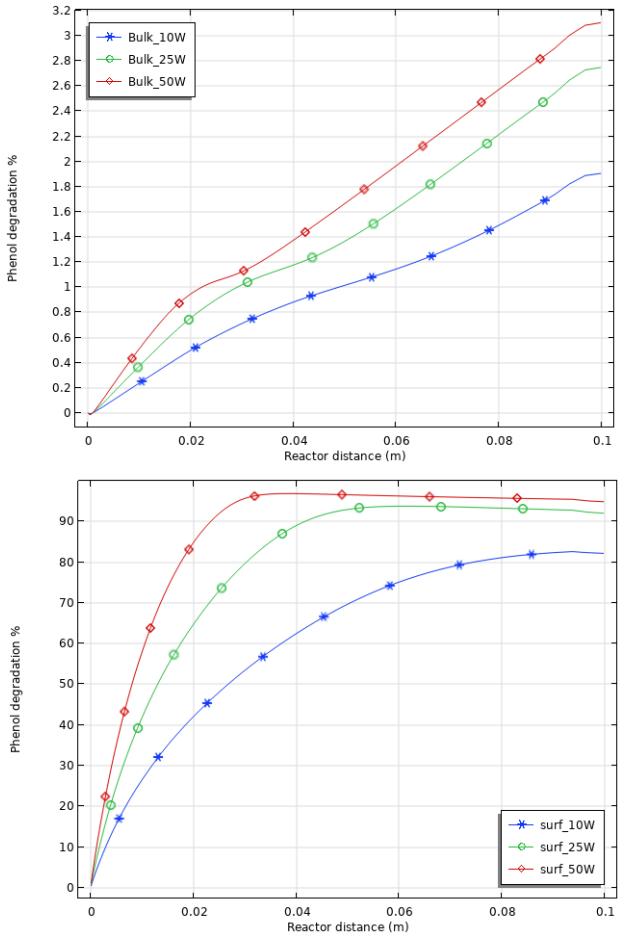

Figure 15.- Power dependence. Conditions: inflow phenol concentration 1mmol/L; catalyst surface concentration 1300 kg/m^3, space velocity 1 min^{-1}. Bulk concentrations (up) and surface concentration (bottom).

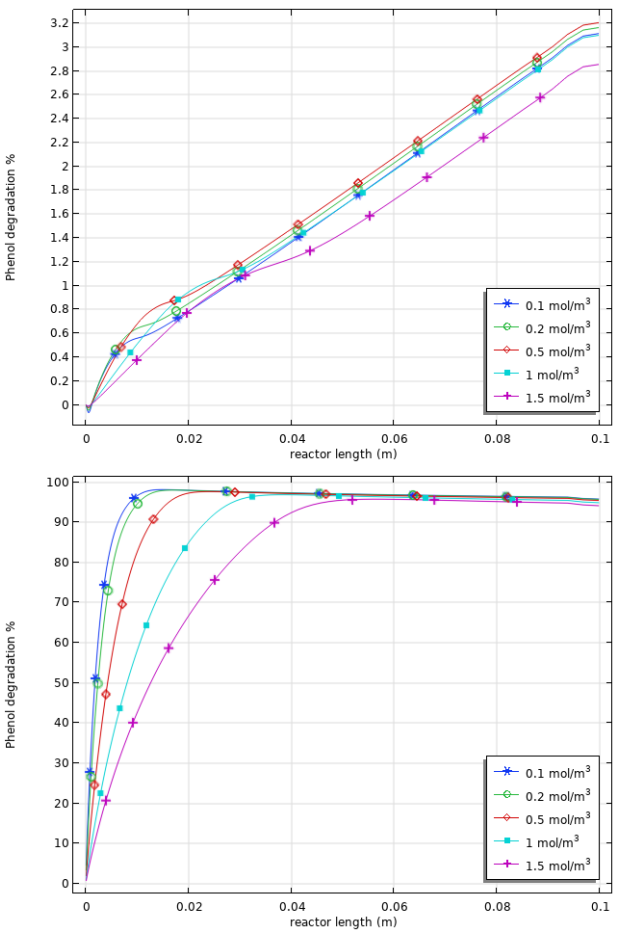

Figure 16.- Phenol inlet concentration dependence. Conditions: lamp power 50W; catalyst surface concentration 1300 kg/m^3, space velocity 1 min^{-1}. Bulk concentrations (up) and surface concentration (bottom).

In figure 17 it appears the catalyst concentration dependence of phenol degradation % for a 50W lamp power, 1mmol/L inlet concentration and 1 min^{-1} space velocity. The reactor shows a higher sensitivity to this parameter although a 10-fold increase in catalyst is needed to double the bulk phenol degradation and to get a 42% increase in surface degradation, while variations in some hundreds of kg/m^3 show a small increase in efficiency.

Figure 18 shows the space velocity dependence of the phenol degradation %. It can be seen that space velocity is the parameter with the highest impact of the ones analyzed. In the case of bulk concentrations, an increase from 1 to 1.5 min^{-1} promotes a degradation decrease of 37.5% and when increasing 10-fold it decreases around a 93%. In the case of surface degradation, the impact is lower for the first 3 space velocity values and also very high for a 5-fold and 10-fold increase over the lowest value. As space velocity is the parameter with the highest impact on phenol degradation it is selected to study its impact on the surface reaction rate.

Figure 19 shows the reaction rate profile along the reactor for the space velocities studied. It can be seen that space velocity has a very low impact on the reaction rates in the upper values of 5 and 10 min^{-1}, while a higher impact can be observed in the lower values. In view of the reaction rate profile, it can be concluded that the reactor of this example is well dimensioned for a space velocity 2 min^{-1}, over dimensioned for 1.5 and 1 min^{-1} and sub dimensioned for 5 and 10 min^{-1}.

Finally, some test on the temperature variation computed from the heat transfer module has been performed. The greatest expected variation is in the surface profile since it is where the source term in equation 23 is not null due to the chemical reactions occurrence. Since space velocity and lamp power were the parameters with greatest impact on surface concentration profile, a parametric study has been performed

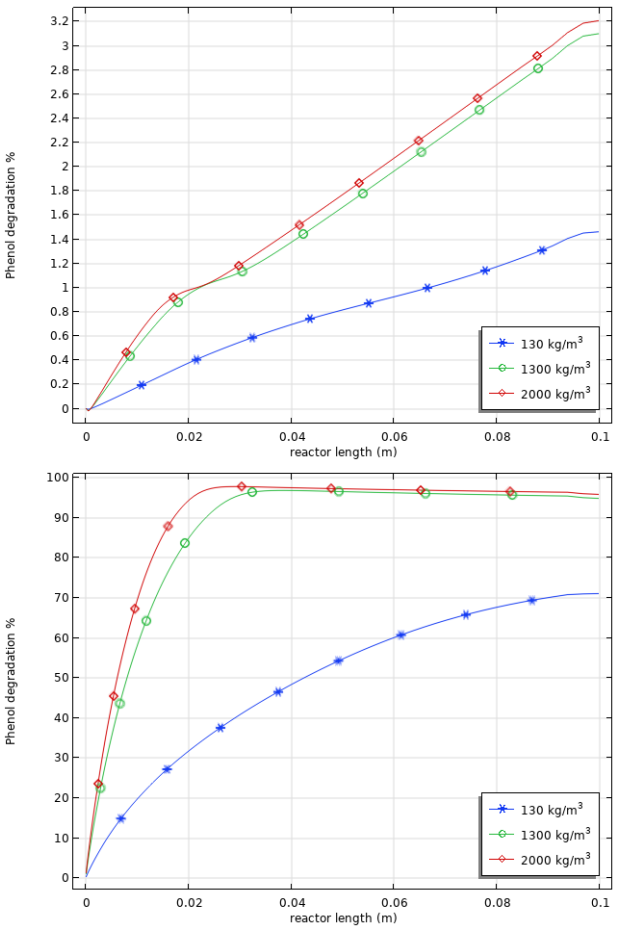

Figure 17.- Catalyst concentration dependence. Conditions: lamp power 50W; inlet concentration 1 mmol/L, space velocity 1 min^{-1}. Bulk concentrations (up) and surface concentration (bottom). along reactor length.

for these parameters. Figures 20 and 21 show the surface T profile in the reactor for space velocity and lamp power sweep respectively. In both simulations, neither parameter seems to have a great impact on T profiles, since T does not appreciably change along the reactor surface except for an order of 10^{-5}-10^{-6} (not appreciated in the plot scale). However, the curves in the plots show a tendency to cool along the reactor. This result was explained in the Heat transfer section of Materials and Methods above.

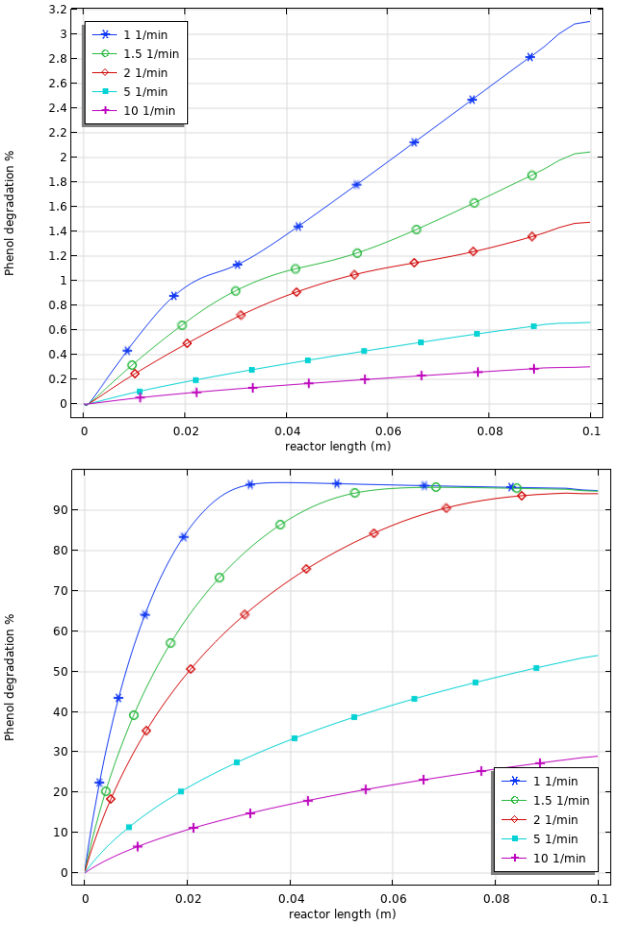

Figure 18.- Space velocity dependence. Conditions: lamp power 50W; inlet concentration 1 mmol/L, catalyst concentration 1300 kg/m^3. Bulk concentrations (up) and surface concentration (bottom).

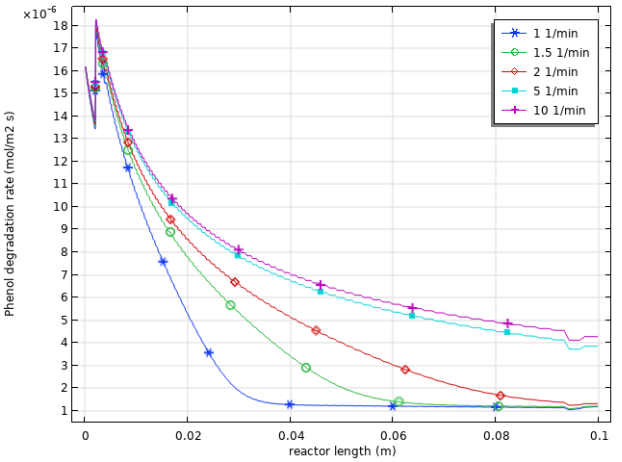

Figure 19.- Space velocity dependence of reaction rate. Conditions: lamp power 50W; inlet concentration 1 mmol/L, catalyst concentration 1300 kg/m^3.

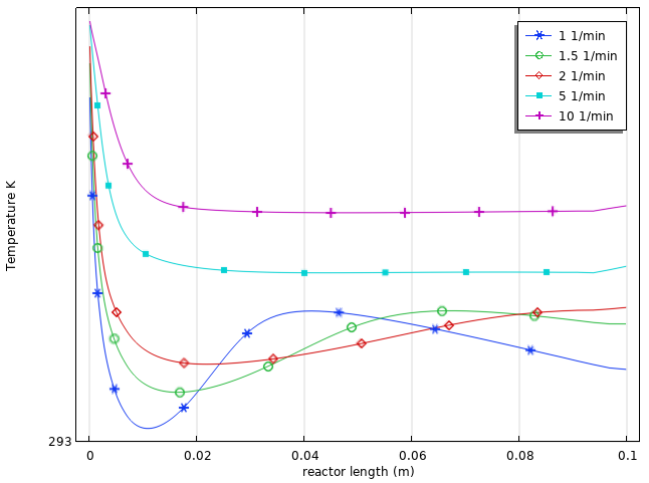

Figure 20.- Space velocity impact on surface T. Conditions: lamp power 50W; inlet concentration 1 mmol/L, catalyst.

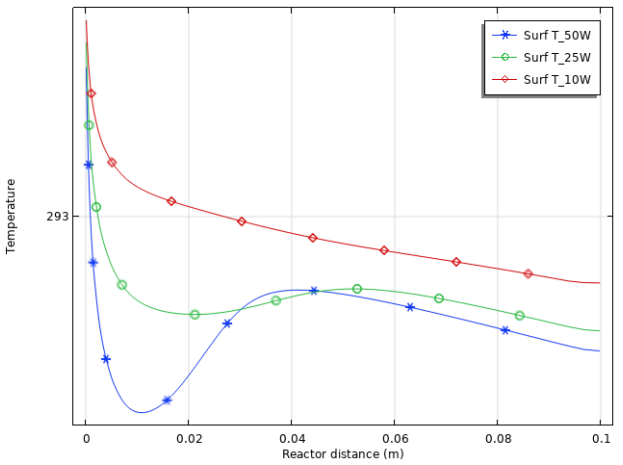

Figure 21.- Lamp power impact on surface T. Conditions: space velocity 1 s^{-1} inlet concentration 1 mmol/L, catalyst

V. CONCLUSIONS

In the present work, an FBPAR model has been built in COMSOL to test the capabilities of this software to theoretically analyze this kind of devices, testing its performance under different conditions. In this case, the phenol degradation efficiency has been tested against different design (power lamp, catalyst surface concentration) and operational (inlet concentration, space velocity) parameters. The model has coupled 5 different physics to account for all the possible effects of different parameters on its performance.

With this model built in COMSOL, it has been possible to show the behavior of a specific reactor design with a specific reaction mechanism in terms of the photodegradation efficiency. It has been possible to show in a quantitative and graphic way the influence of different design and operational parameters like lamp power, catalyst concentration, inlet concentration and space velocity by means of post processing tools like the 3D cut line, which allows to show the phenol concentration (or related values like its degradation %) profiles along specified reactor cut lines. It has also been possible to analyze the reasons of the modelled behavior by means of tools like the 3D plots, surface plots and 2D plots of different reactor cut planes, which made it possible to ascribe the poor performance of the bulk species degradation to the diffusion limitation caused by flow regime.

ACKNOWLEDGMENTS

The authors gratefully acknowledge the technical and academic support of the Multiphysics Modeling School (https://www.multiphysics.uma.es). This study has been financed by PROYMATICA 21 S.L. (https://www.proymatica21.com).

REFERENCES

[1] H. Paul Maruska and Amalk. Ghosh, Photocatalytic Decomposition of Water at Semiconductor Electrodes. *Solar Energy* **20** A3-.458 (1978).

[2] Craig S. Turchi and David F. Ollis. Photocatalytic Degradation of Organic Water Contaminants: Mechanisms Involving Hydroxyl Radical Attack. *Journal of Catalysis* **122**, 178-192 (1990).

[3] A. Alexiadis, G. Baldi, I. Mazzarino. Modelling of a photocatalytic reactor with a fixed bed of supported catalyst. *Catalysis Today* **66** 467–474 (2001).

[4] J. Krysa, K. Bouzek and Ch. Stollberg. Photocatalytic degradation of oxalic acid on a semiconductive layer of n-TiO2 particles in a batch plate reactor. Part III: Rate determining steps and non-steady diffusion model for oxygen transport. *Journal of Applied Electrochemistry* **30** 1033±1041 (2000).

[5] Ringo C.W. Lama, Michael K.H. Leunga, Dennis Y.C. Leunga, Lilian L.P. Vrijmoedb,

W.C. Yamc, S.P. Ngc. Visible-light-assisted photocatalytic degradation of gaseous

formaldehyde by parallel-plate reactor coated with Cr ion-implanted TiO2 thin film. *Solar Energy Materials & Solar Cells.* **91** 54–61 (2007)

[6] Joaquín L. Reyes-García, Camilo A. Arancibia-Bulnes, Fabiola Mendez-Arriaga, Patricio J. Valades-Pelayo, Manuel A. Ramírez Cabrera. Optical and hydrodynamic performance of photocatalytic monoliths of different shapes in a solar photoreactor with compound parabolic collector. *Catalysis Today* **429** 114498 (2024)

[7] María I. Cabrera, Orlando M. Alfano, and Alberto E. Cassano. Absorption and Scattering Coefficients of Titanium

Dioxide Particulate Suspensions in Water. *J. Phys. Chem.*, **100**, 20043-20050 (1996).

[8] Vishnu Pareek, Siewhui Chong, Moses Tadé and Adesoji A. Adesina. Light intensity distribution in heterogenous photocatalytic reactors. *Asia-Pac. J. Chem. Eng.* **3** 171–201 (2008).

[9] O. Alvarado-Rolon, R. Natividad, R. Romero, L. Hurtado, and A. Ramírez-Serrano. Modelling and Simulation of the Radiant Field in an Annular Heterogeneous Photoreactor Using a Four-Flux Model. *International Journal of Photoenergy* 16 (2018).

[10] Siamak Elyasi and Fariborz Taghipour. General method of simulating radiation fields using measured boundary values. *Chemical Engineering Science* **65** 5573–5581 (2010)

[11] Gian Luca Li Puma, Jennee Khor and Alberto Brucato. Modeling of an Annular Photocatalytic Reactor for Water Purification: Oxidation of Pesticides. *Environ. Sci. Technol.* **38** 3737-3745 (2004)

[12] Amélie Queffeulou, Laurent Geron, Eric Schaer. Prediction of photocatalytic air purifier apparatus performances with a CFD approach using experimentally determined kinetic parameters. *Chemical Engineering Science* **65** 5067–5074 (2010).

[13] Siewhui Chong, Shaobin Wang, Moses Tade´, H. Ming Ang, and Vishnu Pareek. Simulations of Photodegradation of Toluene and Formaldehyde in a Monolith Reactor Using Computational Fluid Dynamics. *AIChE Journal* **57** 724-734 (2011)

[14] Frans Denny, Jason Scott, Vishnu Pareek, Gang Ding Peng, Rose Amal. CFD modelling for a TiO2-coated glass-bead photoreactor irradiated by optical fibres: Photocatalytic degradation of oxalic acid. *Chemical Engineering Science* **64** 1695 – 1706 (2009)

[15] A.Tolosana-Moranchel, J.A. Casas, J. Carbajo, M. Faraldos, A. Bahamonde. *Applied Catalysis B: Environmental* **200** 164–173 (2017).

[16] Yash Boyjoo, Ming Ang, Vishnu Pareek. *Chemical Engineering Science* **101** 764–784 (2013).

[17] Ray Optics Module User's Guide. COMSOL 6.2. 1998-2023.

APENDIX I. NOMENCLATURE

Arabic	
R_{ads}	Reaction rates of adsorbed species in the solid phase, mol $m^{-2}s^{-1}$
R_{surf}	Reaction rates of surface species in the solid phase, mol $m^{-2}s^{-1}$
R_r	Rate of electron-hole recombination in solid phase, mol $m^{-2}s^{-1}$
R_h	Reaction rates of hole trapping in the solid phase, mol $m^{-2}s^{-1}$
R_e	Reaction rates of electron trapping in the solid phase, mol $m^{-2}s^{-1}$
R_B	Reaction rates in the bulk phase, mol $m^{-3}s^{-1}$
h_{ads}	Mass transfer coefficient, s^{-1}
k_{rec}	Electron-hole recombination rate constant $m^2\,mol^{-1}\,s^{-1}$
$k^f_{h,i}$	Hole trapping forward rate constant $m^2\,mol^{-1}\,s^{-1}$
$k^r_{h,i}$	Hole trapping reverse rate constant s^{-1}
$k^f_{e,i}$	Electron trapping forward rate constant $m^2\,mol^{-1}\,s^{-1}$
$k^r_{e,i}$	Electron trapping reverse rate constant s^{-1}
k_{OHss}	Hydroxyl attack rate constant of adsorbed species $m^2\,mol^{-1}\,s^{-1}$
k_{OHBs}	Hydroxyl attack rate constant $m^3\,mol^{-1}\,s^{-1}$
k_{OHB}	Hydroxyl attack rate constant of bulk species $m^3\,mol^{-1}\,s^{-1}$
F_v	Fluence rate W m^{-2}
P_v	Ray power, W
$P_{v,a}$	Volumetric rate of photon absorption, W $m^{-2}s^{-1}$
S_{BET}	Catalyst specific surface area m^2g^{-1}
S_A	Catalyst surface area, m^{-1}
A_s	Catalyst supports projected area, m^2
r_g	Surface rate of electron-hole generation, mol $m^{-2}\,s^{-1}$
c_{cat}	Catalyst concentration in the solid phase g m^{-3}
c_v	Volumetric concentration of adsorbed/surface species, mol m^{-3}
c_{eq}	Volumetric equilibrium concentration of adsorbed/surface species, mol m^{-3}
c_p	Surface equilibrium concentration of adsorbed/surface species, mol m^{-2}

c_{ads}	Surface concentration of adsorbed/surface species, mol m^{-2}	ω	Light angular frequency
c_B	Volumetric concentration of bulk species, mol m^{-3}		
u	Flow speed vector, m s^{-1}		
D_B	Diffusion coefficient of bulk species, m^2s^{-1}		
p	Fluid pressure, Pa		
F	Fluid acceleration source vector field, m s^{-2}		
I_v	Light intensity at frequency ν, W m^{-2}		
$k_{v,s}$	Light scattering coefficient at frequency ν, m^{-1}		
$k_{v,a}$	Light absorption coefficient at frequency ν, m^{-1}		
j_v	Light emission coefficient at frequency ν, W m^{-2}		
k	Wave vector		
C_p	Specific heat at constant pressure J/kg·K		
H_r	Enthalpy of reaction J/mol		
Q_{rec}	Heat due to chemical reactions		
Q_{rad}	Heat due to radiative processes		
q	Heat flux		
Greek			
α_1	Rate constant		
α_2	Rate constant		
α_3	Rate constant		
$\bar{\phi}$	Mean quantum yield, mol J^{-1}		
β	Ratio of exposed catalyst surface		
κ	Thermal conductivity		
τ	Viscous stress tensor, Pa		
Ω	Solid angle, stereo-radian		
ρ_B	Bulk phase density kg m^{-3}		
θ	Light incidence angle to a specific point in the reactor		
μ	Cosine of ray incidence angle to a specific point in reactor		
ν	Light frequency		

APENDIX II. PARAMETER VALUES USED IN SIMULATIONS

Name	Value	Description
alpha_1	1.465E-10 mol/(m²·s)	kinetic constant
alpha_2	57.245 s³/kg	kinetic constant
alpha_3	5.45 m³/mol	kinetic constant
F_org_in	9.8175E-8 mol/s	feed organics
F_O2_in	4.9087E-6 mol/s	Feed O2
F_TiO2_in	8.0879E-8 m·mol/s	Feed TiO2
H_Ph	18980 J/mol	Enthalpy of reaction

Table AII.1.- Reaction parameters

Name	Value	Description
L_r	0.1 m	Reactor length
D_r	0.01 m	Reactor diameter
L_l	0.1 m	Lamp length
D_l	0.005 m	Lamp diameter
P_l	25 W	Lamp power
D_fil	0.001 m	Filament diameter
L_fil	0.1 m	Filament length
lambda_l	3E-7 m	Emission wave length

Table AII.2.- Reactor parameters

Name	Value	Description
rho_b	1300 kg/m³	Catalyst bulk density
S_bet	50000 m²/kg	Catalyst BET surface area
S_area	60000 1/m	Catalyst reaction area
c_cat	0.065 kg/m²	Catalyst load
l_cat	5E-5 m	Catalyst layer thickness
M_cat	0.0789 kg/mol	Catalyst molar mass

Table AII.3.- Catalyst parameters

Name	Value	Description
D_O2	2E-9 m²/s	O2 diffussion coefficient in water
D_ph	1E-9 m²/s	Phenol diffussion coefficient in water
D_S	1.2E-9 m²/s	S diffussion coefficient in water

Table AII.4.- Transport parameters

Name	Value	Description
T_iso	525 K	Temperature
c0H2O_inflow	55556 mol/m³	Molar concentration, inflow
c0O2_inflow	50 mol/m³	Molar concentration, inflow
c0org_inflow	1 mol/m³	Molar concentration, inflow
Pf	10 W/m²	Fluence rate
v_in	9.8175E-8 m³/s	Volumetric flow
T_in	293 K	Reaactor inlet temperature
tr	60 s	Hydraulic retention time
Vs	0.016667 1/s	Space velocity

Table AII.5.- Operational parameters